Symmetry origin and microscopic mechanism of electrical magnetochiral anisotropy in tellurium

Manuel Suárez-Rodríguez [1,2] Beatriz Martín-García [1,3] Francesco Calavalle [1] Stepan S. Tsirkin [3,4] Ivo Souza [3,4]
Fernando de Juan [3,5] Albert Fert,[2,5,6] Marco Gobbi [3,4,*] Luis E. Hueso [1,3,†] and Fèlix Casanova [1,3,‡]

[1]*CIC nanoGUNE BRTA, 20018 Donostia–San Sebastián, Basque Country, Spain*
[2]*Department of Polymers and Advanced Materials: Physics, Chemistry and Technology UPV/EHU,*
20018 Donostia–San Sebastián, Basque Country, Spain
[3]*IKERBASQUE, Basque Foundation for Science, 48009 Bilbao, Basque Country, Spain*
[4]*Centro de Física de Materiales CSIC-UPV/EHU, 20018 Donostia–San Sebastián, Basque Country, Spain*
[5]*Donostia International Physics Center, 20018 Donostia–San Sebastián, Basque Country, Spain*
[6]*Laboratoire Albert Fert, CNRS, Thales, Université Paris-Saclay, 91767 Palaiseau, France*

Nonlinear transport effects in response to external magnetic fields, i.e., electrical magnetochiral anisotropy (eMChA), have attracted much attention for their importance in studying quantum and spin-related phenomena. Indeed, they have permitted the exploration of topological surface states and charge to spin conversion processes in low-symmetry systems. Nevertheless, despite the inherent correlation between the symmetry of the material under examination and its nonlinear transport characteristics, there is a lack of experimental demonstration to delve into this relationship and to unveil their microscopic mechanisms. Here, we study eMChA in chiral elemental tellurium (Te) along different crystallographic directions, establishing the connection between the different eMChA components and the crystal symmetry of Te. We observed different longitudinal eMChA components with collinear current and magnetic field, demonstrating experimentally the radial angular momentum texture of Te. We also measured a transverse nonlinear resistance which, as the longitudinal counterpart, scales bilinearly with current and magnetic fields, illustrating that they are different manifestations of the same effect. Finally, we study the scaling law of the eMChA, evidencing that extrinsic scattering is the dominant microscopic mechanism. These findings underscore the efficacy of symmetry-based investigations in understanding and predicting nonlinear transport phenomena, with potential applications in spintronics and energy harvesting.

I. INTRODUCTION

Low-symmetry materials have revolutionized the field of electronic transport. This disruption stems from the breaking of inversion symmetry within such systems, which permits nonlinear transport effects where the voltage (V) scales quadratically with the current (I) [1]. Notably, this nonlinear behavior can manifest both with and without the presence of external magnetic fields (B) [2].

On the one hand, nonlinear transport effects in the absence of B ($I \propto V^2$) have recently attracted much attention [3–6]. Indeed, they allowed for the study of novel quantum properties, such as the Berry curvature [7,8] or Berry connection polarizability [9,10], and have the potential to be exploited for energy harvesting through radio-frequency rectification [11–14]. Systematic studies have been performed, identifying both longitudinal (i.e., nonlinear conductivity [15,16]) and transverse (i.e., nonlinear Hall effect (NLHE) [3,4,17]) components, and its connection with the crystal symmetry of the tested material.

On the other hand, nonlinear transport effects in the presence of B ($I \propto V^2 B$) have great importance for spintronics as they can be employed for the investigation of spin-related effects [18]. In general, these phenomena are named electrical magnetochiral anisotropy (eMChA) [19,20]. However, as most reports are focused on the longitudinal manifestation, they are commonly known as unidirectional magnetoresistance (UMR) [18] or bilinear magnetoresistance (BMR) [21,22]. Although there are a few reports on the transverse manifestation, i.e., nonlinear planar Hall effect (NLPHE) [23,24], an experimental demonstration of the fundamental connection between the two effects and the crystal symmetry of the material is still absent. Furthermore, the microscopic mechanisms behind these effects remain unclear.

Chiral materials provide an exceptional platform for investigating nonlinear transport effects due to their absence of both inversion and mirror symmetry [25–27]. In this context, a material with strong spin-orbit coupling such as chiral tellurium (Te) [28], which can be chemically synthesized [29] and patterned into desired shapes, emerges as the ideal candidate.

In this paper, we present an experimental study of eMChA in Te, encompassing both longitudinal and transverse measurements, along with an analysis of the crystallographic direction dependence. Te flakes are grown via a hydrothermal process and patterned into star-shaped structures, enabling

---

*Contact author: marco.gobbi@ehu.eus
†Contact author: l.hueso@nanogune.eu
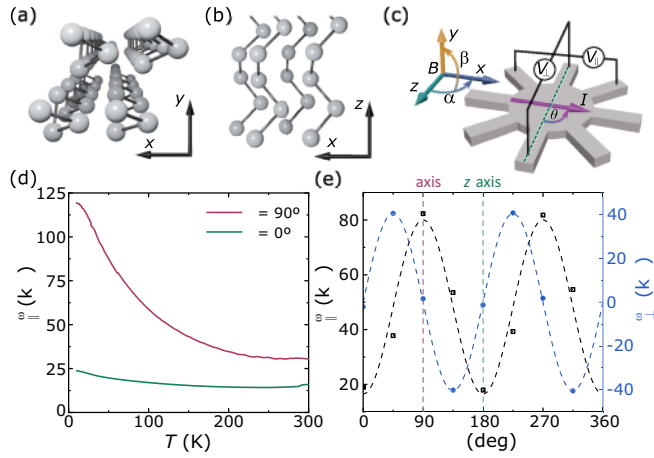‡Contact author: f.casanova@nanogune.eu

FIG. 1. Anisotropic transport in Te. (a), (b) Crystal structure sketch of trigonal Te in the (a) $x - y$ and (b) $x - z$ plane. (c) Sketch of the star-shaped Te device. The relative orientation between B and the device is indicated. (d) Temperature dependence of $R_\parallel$ when I is injected along the x ($\theta = 90°$) and z axis ($\theta = 0°$). (e) $R_\parallel$ and $R_\perp$ as a function of θ at 50 K. The dashed lines are fits to the equations introduced in the main text. The $R_\parallel$ and $R_\perp$ values are obtained from the linear fittings in Fig. S1 [30]. All measurements were performed at $B = 0$ T with $|I| = 1\,\mu$A.

precise measurements along different crystallographic directions. By taking into account the symmetry of trigonal Te, we derive equations that accurately describe the experimental nonlinear transport in Te across all configurations. We observe a longitudinal eMChA, i.e., UMR or BMR, when B and I are aligned along the z axis, consistent with previous reports [18]. Remarkably, we also observe a longitudinal eMChA when both B and I are along the x axis, thus demonstrating the anisotropic radial angular momentum texture of Te by electrical means. Additionally, we detect a transverse eMChA, i.e., NLPHE, when B is along the z axis and I is along the x axis. We illustrate that this transverse nonlinear resistance exhibits bilinear dependence on B and I. Finally, by examining the dependence of the eMChA on the resistivity, we establish that the eMChA in Te is primarily governed by extrinsic mechanisms. Our findings underscore how the analysis of crystal symmetry and resistivity scaling facilitate the prediction of nonlinear transport effects, providing insights into permitted components and microscopic mechanisms. Therefore, we aim to inspire similar analyses devoted to discovering novel systems suitable for spintronics and energy harvesting applications.

II. ANISOTROPIC TRANSPORT

Trigonal elemental Te displays a chiral crystal structure, belonging to $P3_121$ (right-handed) or $P3_221$ (left-handed) space groups [Figs. 1(a) and 1(b)]. We grow single crystalline Te flakes following a hydrothermal process [29], and we pattern them into a star-shaped device by e-beam lithography and reactive ion etching. Finally, we contact them with Pt electrodes allowing electrical measurements for different

crystallographic directions (Supplemental Material, Sec. 1 [30]; also see [31–35]). A harmonic current at frequency $=$ 31 Hz (I) is injected between two electrodes aligned in the same direction at a θ angle from the chiral z axis. During this process, both the first- (V) and second- ($V^{2\omega}$) harmonic voltages are recorded. The measurements are conducted in both longitudinal ($V_\parallel$) and transverse ($V_\perp$) configurations using a rotating reference frame. Our setup also enables temperature modulation (2–300 K) and the application of B up to 9 T in all directions [Fig. 1(c)].

Figure 1(d) shows the temperature dependence of the first-harmonic longitudinal resistance ($R_\parallel \equiv \frac{V_\parallel}{I}$) along the z axis ($\theta = 0°$) as well as the x axis ($\theta = 90°$). We note that the resistance along the x axis is much higher than along the z axis, which is a direct consequence of the anisotropic crystal structure: the electronic transport is much more favorable along the covalently bonded Te helices (z axis) than between them (x axis). To further study the anisotropic electronic transport in Te and to ensure proper control of current directionality, we measure the first-harmonic longitudinal ($R_\parallel$) and transverse resistance ($R_\perp \equiv \frac{V_\perp}{I}$) for different θ angles, between the current I and the chiral z axis [Fig. 1(e)]. On the one hand, $R_\parallel$ follows $R_\parallel(\theta) = (L_\parallel/A)[\rho_{zz}\cos^2(\theta) + \rho_{xx}\sin^2(\theta)]$, where $L_\parallel$ is the distance between longitudinal contacts, A is the cross section of the contacts, and ρ_{zz} and ρ_{xx} are the resistivities along the z and x axis, respectively. We observe that $\rho_{xx} \gg \rho_{zz}$, in agreement with the temperature dependence study [Fig. 1(d)]. On the other hand, $R_\perp$ follows $R_\perp(\theta) = (L_\perp/A)(\rho_{xx} - \rho_{zz})\cos(\theta)\sin(\theta)$, where $L_\perp$ is the distance between transverse contacts. The excellent fittings of the experimental data to the expected θ dependence indicate precise control of the current directionality in our devices, allowing for further crystallographic-dependent transport experiments (see Supplemental Material, Sec. 2 [30]).

III. ANISOTROPIC MAGNETOTRANSPORT

Recently, the electronic transport properties of Te in response to B have attracted much attention. Negative magnetoresistance [18,36] and planar Hall effect [37] have been reported, both being considered as possible signatures of Weyl physics [37]. However, it is worth noting that the Weyl points in trigonal Te are at ∼0.4 and 0.5 eV below the top of the valence band [38], thus far away from where the electronic transport generally occurs [39]. In the following, we will demonstrate that, from crystal symmetry considerations, it is possible to analyze the different magnetoresistance and Hall components in trigonal Te.

The first-order electric field (E_i) in response to a current density (j_j) and a magnetic field ($B_{k,l}$) can be expressed through the material magnetoresistance (T_{ijkl}) and Hall (R_{ijk}) tensors as $E_i = T_{ijkl}j_j B_k B_l + R_{ijk}j_j B_k$. We observe that the magnetoresistance and Hall contributions are even and odd, respectively, with respect to $B_{k,l}$. Therefore, it is possible to differentiate them experimentally. For Te, considering E_i and j_j in the $x - z$ plane and $B_{k,l}$ in all directions, the magnetoresistance and Hall tensors have nine and two nonzero
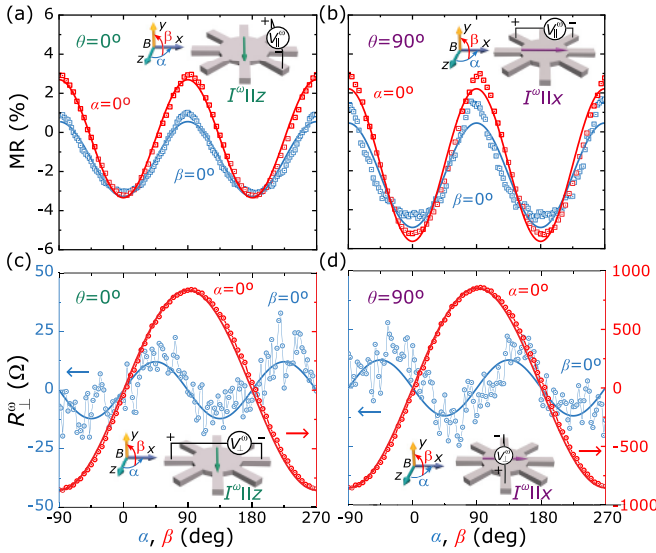
FIG. 2. Anisotropic magnetotransport in Te. (a), (b) Te MR as a function of α angle ($\beta = 0°$, blue curve) and β angle ($\alpha = 0°$, red curve) when I is along the (a) z axis ($\theta = 0°$) and (b) x axis ($\theta = 90°$). (c), (d) $R_\perp$ as a function of α angle ($\beta = 0°$, blue curve) and β angle ($\alpha = 0°$, red curve) when I is along the (c) z axis ($\theta = 0°$) and (d) x axis ($\theta = 90°$). All measurements were performed at 50 K and $B = 9$ T. The solid lines are fits to Eqs. (3)–(6).

elements, respectively [40]:

$$T_{ijkl}^{Te} = \begin{pmatrix} T_{xxxx} & T_{xxyy} & T_{xxzz} & T_{xxyz} & 0 & 0 \\ T_{zzxx} & T_{zzyy} & T_{zzzz} & 0 & 0 & 0 \\ 0 & 0 & 0 & 0 & T_{xzxz} & T_{xzxy} \end{pmatrix}, \quad (1)$$

$$R_{ijk}^{Te} = \begin{pmatrix} 0 & 0 & 0 \\ 0 & R_{xzy} & 0 \\ 0 & -R_{xzy} & 0 \\ 0 & 0 & 0 \end{pmatrix}. \quad (2)$$

Therefore, we can obtain the expressions of the longitudinal and transverse electric fields as a function of θ, α, and β angles in terms of T_{ijkl} and R_{ijk} (see Supplemental Material, Sec. 2 [30]). To disentangle the different components, we have measured the Te magnetoresistance (MR $\equiv \frac{R_\parallel(B=9T)-R_\parallel(B=0T)}{R_\parallel(B=0T)}$) for $\theta = 0°$ [Fig. 2(a)] and $\theta = 90°$ [Fig. 2(b)], and also $R_\perp$ for $\theta = 0°$ [Fig. 2(c)] and $\theta = 90°$ [Fig. 2(d)], by rotating $B = 9$ T in both the α and β planes [Fig. 1(c)].

Figures 2(a) and 2(b) manifest that the equations obtained from our analysis based on Te crystal symmetry perfectly capture the experimental response, both for the α-angle dependence (blue curves),

$$\text{MR} = (B^2/\rho_{zz})\cos^2(\theta)[T_{zzxx}\sin^2(\alpha) + T_{zzzz}\cos^2(\alpha)]$$
$$+ (B^2/\rho_{xx})\sin^2(\theta)[T_{xxxx}\sin^2(\alpha) + T_{xxzz}\cos^2(\alpha)], \quad (3)$$

and for the β-angle dependence (red curves),

$$\text{MR} = (B^2/\rho_{zz})\cos^2(\theta)[T_{zzyy}\sin^2(\beta) + T_{zzzz}\cos^2(\beta)]$$
$$+ (B^2/\rho_{xx})\sin^2(\theta)[T_{xxyz}\sin(\beta)\cos(\beta) + T_{xxyy}\sin^2(\beta)$$
$$+ T_{xxzz}\cos^2(\beta)] \quad (4)$$

(see Supplemental Material, Sec. 2 [30]). Importantly, we recognized that the critical parameter for the MR is the direction of the magnetic field. The MR is negative when B is along the z axis ($\alpha = \beta = 0°$), independently on the direction of I (see also Figs. S2(a) and S2(b) [30]). Previous reports have studied the magnetotransport of Te only when I is along the z axis, and related its negative MR with the chiral anomaly [37]. However, the chiral anomaly can only apply for $B \parallel I$ [41], and we also observe negative MR when $B \perp I$. Therefore, our observation suggests a different mechanism behind the negative MR in Te, such as Berry curvature or orbital moments [42–45]. A temperature dependence of the MR can be found in Figs. S2(c) and S2(d) [30].

Regarding the transverse measurements [Figs. 2(c) and 2(d)], we observe that the β-angle dependence ($\alpha = 0°$, red curves) is given by the Hall component:

$$R_\perp = (L_\parallel/A)R_{xzy}B\sin(\beta)[\sin^2(\theta) + \cos^2(\theta)]. \quad (5)$$

Indeed, when the magnetic field is out of plane ($B \parallel y$ axis) we detect the ordinary Hall effect in Te, whose sign and magnitude indicate that the electronic transport is dominated by holes and permits one to obtain the carrier density $n_h \approx 6.5 \times 10^{17}$ cm^{-3} (Figs. S2(e) and S2(f) [30]). For the α-angle dependence ($\beta = 0°$, blue curves), we observe the so-called planar Hall effect:

$$R_\perp = -2(L_\perp/A)T_{xzxz}B^2\sin(\alpha)\cos(\alpha)[\sin^2(\theta) - \cos^2(\theta)]. \quad (6)$$

The planar Hall effect is even with respect to B, and thus is not a true Hall effect [46]. The planar Hall effect has been considered a signature of Weyl physics [37], but we demonstrate that it is directly allowed by the symmetry of Te and its associated MR tensor (T_{xzxz} component). Therefore, as for the negative MR, its origin may be related to Berry curvature or orbital moments. More importantly, the equations obtained from the analysis of Te symmetry perfectly capture all the experimental observations (solid lines in Fig. 2), demonstrating that it is a powerful method. From the fittings of the experimental data, we determined the values of the resistivity, magnetoresistance, and Hall tensor components (Table S1 [30]).

IV. ELECTRICAL MAGNETOCHIRAL ANISOTROPY

Nonlinear transport effects in response to external magnetic fields, i.e., eMChA, have attracted much attention for their importance in spintronics. Indeed, eMChA has been reported in two-dimensional electron gases [22] and topological insulators [21], unveiling the helical spin texture of these systems. Recently, eMChA has also been reported in elemental Te [18]. The symmetry of chiral Te gives rise to an anisotropic handedness-dependent radial spin texture [28,47], which is compatible with the eMChA experiments. Therefore, the eMChA measurements can be exploited to determine the handedness of Te crystals [18]. These experiments have been limited to currents along the chiral z axis. However, the Te chiral structure offers a rich family of eMChA components [20] that can be investigated with our star-shaped Te devices.

In general, the second-order current density (j_i^2) in response to an electric ($E_{j,k}$) and magnetic (B_l) field can be expressed through the eMChA conductivity tensor (σ_{ijkl}) of
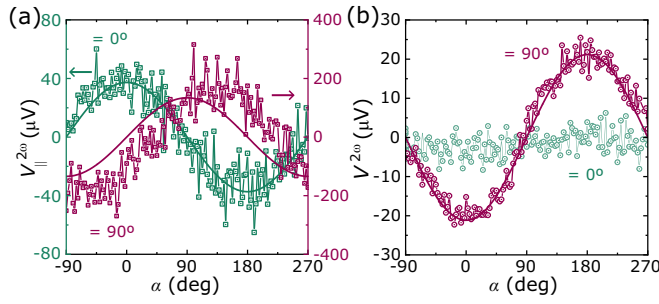
FIG. 3. Crystallographic direction dependence of eMChA in Te. (a) $V_\parallel^{2\omega}$ and (b) $V_\perp^{2\omega}$ when I is along the z axis ($\theta = 0°$, green curve) and the x axis ($\theta = 90°$, magenta curve) as a function of α angle at 9 T and $\beta = 0°$. All measurements were performed at 50 K with $|I| = 1\,\mu A$. The solid lines are fits of the experimental data to Eqs. (8)–(11).

the material as $j_i^2 = \sigma_{ijkl} E_j E_k B_l$. For Te, considering $E_{j,k}$ and j_i^2 in the $x - z$ plane and B_l in all directions, the eMChA conductivity tensor has eight independent nonzero elements [40]:

$$\sigma_{ijkl} = \begin{pmatrix} \sigma_{xxxx} & \sigma_{xzzx} & 0 \\ 0 & 0 & \sigma_{xxzy} \\ 0 & 0 & \sigma_{xxzz} \\ 0 & 0 & \sigma_{zxzx} \\ \sigma_{zxxy} & 0 & 0 \\ \sigma_{zxxz} & \sigma_{zzzz} & 0 \end{pmatrix}. \quad (7)$$

As in the previous section, we can measure both the longitudinal and transverse response when I is along the z axis ($\theta = 0°$) and x axis ($\theta = 90°$). For such current directions, the longitudinal second-harmonic voltage ($V_\parallel^{2\omega}$) is given by (for more details, see Supplemental Material, Sec. 3 [30]) the following equations:

$$\theta = 0° \quad V_\parallel^{2\omega} = -\frac{L_\parallel}{A^2}(I^\omega)^2 \rho_{zz}^3 \sigma_{zzzz} B \cos(\alpha)\cos(\beta), \quad (8)$$

$$\theta = 90° \quad V_\parallel^{2\omega} = -\frac{L_\parallel}{A^2}(I^\omega)^2 \rho_{xx}^3 \sigma_{xxxx} B \sin(\alpha)\cos(\beta). \quad (9)$$

To explore the longitudinal components, we recorded $V_\parallel^{2\omega}$ as a function of the α angle at $B = 9$ T and $\beta = 0°$ [Fig. 3(a)]. For $I \parallel z$ axis ($\theta = 0°$), the maximum signal is when B and I are collinear ($B \parallel I \parallel z$), as indicated by Eq. (8) and in agreement with previous reports [18]. Interestingly, for $I \parallel x$ axis ($\theta = 90°$), the maximum signal is also when B and I are collinear ($B \parallel I \parallel x$), as predicted by Eq. (9). Therefore, these results demonstrate the radial angular momentum texture of Te by purely electrical means. The eMChA is maximum when the external magnetic field is parallel to the current-induced angular momentum accumulation (J_i), which points along the z axis when the current is along the z axis ($J_z \parallel I \parallel z$), and points along the x axis when the current is along the x axis ($J_x \parallel I \parallel x$). The longitudinal eMChA is usually related to the spin texture of the system [21,22]. However, recent theoretical works suggest that the orbital contribution may be dominant [48]. Indeed, theoretical predictions indicate that, in Te, the orbital (L_i) is stronger than the spin component (S_i) and, thus, dictates the eMChA response [20,49].

Therefore, as they have the same symmetry and we cannot distinguish between them in our experiments, we have decided to use the term "angular momentum texture" to account for both contributions ($J_i = L_i + S_i$). From the fittings, we obtain the values of $\sigma_{xxxx} = (-5.31 \pm 0.48)10^{-6} \text{AV}^{-2}\text{T}$ and $\sigma_{zzzz} = (-1.283 \pm 0.048)10^{-4} \text{AV}^{-2}\text{T}$. The substantial difference between the magnitudes of σ_{xxxx} and σ_{zzzz} indicates that the angular momentum texture of Te is not merely radial but also anisotropic.

The transverse eMChA, i.e., NLPHE, has been much less studied in the literature [23,24]. Indeed, current direction-dependent studies, which identify the connections between the eMChA components and the crystal symmetry of the studied material, are still absent. Here, we employ our analysis based on Te symmetry, which determines that the transverse second-harmonic voltage ($V_\perp^{2\omega}$) is given by (see Supplemental Material, Sec. 3 [30]) the following equations:

$$\theta = 0° \quad V_\perp^{2\omega} = -\frac{L_\perp}{A^2}(I^\omega)^2 \rho_{xx}\rho_{zz}^2 \sigma_{xzzx} B \sin(\alpha)\cos(\beta), \quad (10)$$

$$\theta = 90° \quad V_\perp^{2\omega} = -\frac{L_\perp}{A^2}(I^\omega)^2 \rho_{xx}^2 \rho_{zz} B[\sigma_{zxxz}\cos(\alpha)\cos(\beta) + \sigma_{zxxy}\sin(\beta)]. \quad (11)$$

Hence, to explore the transverse components, we record $V_\perp^{2\omega}$ as a function of the α angle at $B = 9$ T [Fig. 3(b)]. We note that, in the α-angle dependence at $\beta = 0°$, the component σ_{zxxy} does not contribute [see Eq. (11)]. Remarkably, we observe a clear eMChA signal when $I \parallel x$ (magenta curve, $\theta = 90°$) but not when $I \parallel z$ (green curve, $\theta = 0°$). Assuming σ_{zxxz} and σ_{xzzx} to be of the same order of magnitude, $V_\perp^{2\omega}$ is expected to be larger for $I \parallel x$, because $\rho_{xx} \gg \rho_{zz}$ [see Eqs. (10) and (11)]. Moreover, $V_\perp^{2\omega}$ in response to I and B has also a contribution coming from a combination of nonlinear conductivity and ordinary Hall. For $\beta = 0°$, this extra contribution has no impact when $I \parallel x$ but does have one when $I \parallel z$ and, therefore, it may cancel out the eMChA component (see Supplemental Material, Sec. 4 [30]). From the fitting to Eq. (11), we quantify the value of $\sigma_{zxxz} = (2.603 \pm 0.039)10^{-6} \text{AV}^{-2}\text{T}$. More importantly, for both longitudinal and transverse measurements, our symmetry analysis perfectly captures the experimental response (solid lines in Fig. 3), unveiling the relationships between voltage, current, and magnetic field directions for which the eMChA in Te is allowed.

We further explore the transverse eMChA, by studying its current, field, and temperature dependence. The longitudinal eMChA, when defined as a resistance ($R_\parallel^{2\omega} = V_\parallel^{2\omega}/I^\omega$), is commonly known as BMR because it depends linearly on I and B [Eqs. (8) and (9)]. However, as dictated by Eqs. (10) and (11), the transverse nonlinear resistance ($R_\perp^{2\omega} = V_\perp^{2\omega}/I^\omega$) is also expected to depend linearly on both. To prove this, we record $V_\perp^{2\omega}$ for different I^ω at $B = 9$ T [Fig. 4(a)] and for different B at $|I| = 1\,\mu A$ [Fig. 4(b)], as a function of the β angle at $\alpha = 0°$ and $\theta = 90°$. We note that, to fully demonstrate the accuracy of our symmetry analysis, we have studied $V_\perp^{2\omega}$ as a function of the α angle in Fig. 3 and as a function of the β angle in Fig. 4. As observed, the experimental behavior of $V_\perp^{2\omega}$ is perfectly captured by Eq. (11), and $R_\perp^{2\omega}$ depends bilinearly on current and magnetic field [insets in
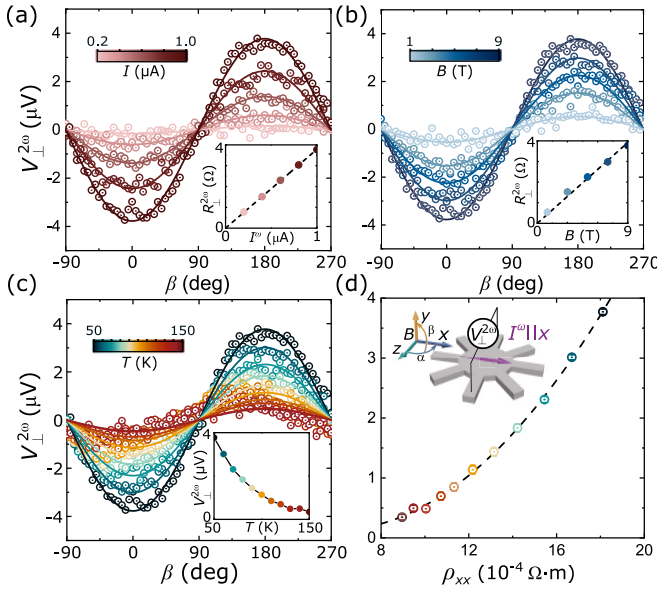
FIG. 4. Current, field, and temperature dependence of the eMChA in Te. (a)–(c) $V_\perp^2$ when I is along the x axis ($\theta = 90°$) as a function of β angle for (a) different I at $B = 9$ T and $T = 50$ K, (b) different B at $T = 50$ K and $|I| = 1\,\mu$A, and (c) different T at $B = 9$ T and $|I| = 1\,\mu$A. (d) $V_\perp^2$ when I is along the x axis ($\theta = 90°$), obtained from the fittings in panel (c) to Eq. (11), as a function of ρ_{xx}. The dashed line is a fit to Eq. (12). Insets: (a) I and (b) B dependence of $R_\perp^2 = V_\perp^2 / I$, (c) T dependence of $V_\perp^2$. The values have been obtained from the fittings in panels (a)–(c) to Eq. (11). (d) Sketch of the measurement configurations.

Figs. 4(a) and 4(b)]. The same bilinear dependence is obtained with the results as a function of the α angle (Fig. S3 [30]), providing further evidence of the accuracy of our symmetry analysis. Equation (11) includes a term $\sigma_{zxxy}\sin(\beta)$, but experimentally no $\sin(\beta)$ dependence is observed. The reason may be that σ_{zxxy} is negligible with respect to σ_{zxxz} or its impact on $V_\perp^2$ could be canceled out by the contribution of the nonlinear conductivity combined with the ordinary Hall effect, which is also allowed for $\theta = 90°$ with the same $\sin(\beta)$ dependence (see Supplemental Material, Sec. 4 [30]).

Finally, we studied the microscopic mechanism of the eMChA [2]. For that purpose, we adapted the analysis developed for time-odd nonlinear transport in magnetic systems [50]. Indeed, the external magnetic field in eMChA plays a similar role to the internal magnetic vectors in time-odd nonlinear transport within magnetic systems. However, in the eMChA analysis, the orbital magnetic field contributions must

also be included [20] (for more details, see Supplemental Material, Sec. 5 [30]). The procedure relies on examining the scaling law between the output voltage, in this case $V_\perp^2$, and the resistivity of the material, ρ_{xx},

$$\frac{V_\perp^2}{(I)^2} = \gamma \rho_{xx}^{-1} + \delta + \xi \rho_{xx} + \zeta \rho_{xx}^2 + \eta \rho_{xx}^3, \qquad (12)$$

where η is a resistivity-independent parameter, while γ, δ, ξ, and ζ only depend on the residual resistivity of the material. The intrinsic contributions of the eMChA are included in the ξ and η parameters (see Supplemental Material, Sec. 5 [30]). To explore the eMChA scaling law in our Te device, we modulate the resistivity by varying T [Fig. 1(d)]. Within this T range, we recorded $V_\perp^2$ for I along the x axis ($\theta = 90°$) as a function of the β angle at $B = 9$ T and $\alpha = 0°$ [Fig. 4(c)]. Hence we can now represent $V_\perp^2$ as a function of T [inset in Fig. 4(c)] and, thus, as a function of ρ_{xx} [Fig. 4(d)]. By fitting the experimental data to Eq. (12), we discern that the ζ term dominates, demonstrating that an extrinsic mechanism governs the eMChA in Te (see Supplemental Material, Sec. 5 [30]). We performed the same analysis for the longitudinal eMChA with I along the z axis ($\theta = 0°$), obtaining the same conclusions (Fig. S4, Table S2 [30]). Therefore, we have successfully identified the dominant microscopic mechanism in our Te devices. This methodology paves the way for similar analyses to uncover the microscopic mechanisms behind eMChA in a wide range of noncentrosymmetric systems.

[1] T. Ideue and Y. Iwasa, Symmetry breaking and nonlinear electric transport in van der Waals nanostructures, Annu. Rev. Condens. Matter Phys. **12**, 201 (2021).

[2] M. Suárez-Rodríguez, F. de Juan, I. Souza, M. Gobbi, F. Casanova, and L. E. Hueso, Non-linear transport in noncentrosymmetric systems: From fundamentals to applications, arXiv:2412.05253.

[3] Q. Ma, S.-Y. Xu, H. Shen, D. MacNeill, V. Fatemi, T.-R. Chang, A. M. Mier Valdivia, S. Wu, Z. Du, C.-H. Hsu

et al., Observation of the nonlinear Hall effect under time-reversal-symmetric conditions, Nature (London) **565**, 337 (2019).

[4] K. Kang, T. Li, E. Sohn, J. Shan, and K. F. Mak, Nonlinear anomalous Hall effect in few-layer WTe$_2$, Nat. Mater. **18**, 324 (2019).

[5] Z. Z. Du, C. M. Wang, S. Li, H. Z. Lu, and X. C. Xie, Disorder-induced nonlinear Hall effect with time-reversal symmetry, Nat. Commun. **10**, 3047 (2019).

[6] Z. Z. Du, C. M. Wang, H. P. Sun, H. Z. Lu, and X. C. Xie, Quantum theory of the nonlinear Hall effect, Nat. Commun. **12**, 5038 (2021).

[7] J. Xiao, Y. Wang, H. Wang, C. D. Pemmaraju, S. Wang, P. Muscher, E. J. Sie, C. M. Nyby, T. P. Devereaux, X. Qian *et al.*, Berry curvature memory through electrically driven stacking transitions, Nat. Phys. **16**, 1028 (2020).

[8] T. Nishijima, T. Watanabe, H. Sekiguchi, Y. Ando, E. Shigematsu, R. Ohshima, S. Kuroda, and M. Shiraishi, Ferroic Berry curvature dipole in a topological crystalline insulator at room temperature, Nano Lett. **23**, 2247 (2023).

[9] A. Gao, Y.-F. Liu, J.-X. Qiu, B. Ghosh, T. V. Trevisan, Y. Onishi, C. Hu, T. Qian, H.-J. Tien, S.-W. Chen *et al.*, Quantum metric nonlinear Hall effect in a topological antiferromagnetic heterostructure, Science **381**, 181 (2023).

[10] N. Wang, D. Kaplan, Z. Zhang, T. Holder, N. Cal, A. Wang, X. Zhou, F. Zhou, Z. Jiang, C. Zhang *et al.*, Quantum-metric-induced nonlinear transport in a topological antiferromagnet, Nature (London) **621**, 487 (2023).

[11] H. Isobe, S. Y. Xu, and L. Fu, High-frequency rectification via chiral Bloch electrons, Sci. Adv. **6**, eaay2497 (2020).

[12] D. Kumar, C.-H. Hsu, R. Sharma, T.-R. Chang, P. Yu, J. Wang, E. Goki, G. Liang, and H. Yang, Room-temperature nonlinear Hall effect and wireless radiofrequency rectification in Weyl semimetal TaIrTe$_4$, Nat. Nanotechnol. **16**, 421 (2021).

[13] M. Suárez-Rodríguez, B. Martín-García, W. Skowroński, K. Staszek, F. Calavalle, A. Fert, M. Gobbi, F. Casanova, and L. E. Hueso, Microscale chiral rectennas for energy harvesting, Adv. Mater. **36**, 2400729 (2024).

[14] X. F. Lu, C. P. Zhang, N. Wang, D. Zhao, X. Zhou, W. Gao, X. H. Chen, K. T. Law, and K. P. Loh, Nonlinear transport and radio frequency rectification in BiTeBr at room temperature, Nat. Commun. **15**, 245 (2024).

[15] P. He, G. K. W. Koon, H. Isobe, J. Y. Tan, J. Hu, A. H. C. Neto, L. Fu, and H. Yang, Graphene moiré superlattices with giant quantum nonlinearity of chiral Bloch electrons, Nat. Nanotechnol. **17**, 378 (2022).

[16] M. Suárez-Rodríguez, B. Martín-García, W. Skowroński, F. Calavalle, S. S. Tsirkin, I. Souza, F. de Juan, A. Chuvilin, A. Fert, M. Gobbi *et al.*, Odd nonlinear conductivity under spatial inversion in chiral tellurium, Phys. Rev. Lett. **132**, 046303 (2024).

[17] A. Tiwari, F. Chen, S. Zhong, E. Drueke, J. Koo, A. Kaczmarek, C. Xiao, J. Gao, X. Luo, Q. Niu *et al.*, Giant *c*-axis nonlinear anomalous Hall effect in T_d-MoTe$_2$ and WTe$_2$, Nat. Commun. **12**, 2049 (2021).

[18] F. Calavalle, M. Suárez-Rodríguez, B. Martín-García, A. Johansson, D. C. Vaz, H. Yang, I. V. Maznichenko, S. Ostanin, A. Mateo-Alonso, A. Chuvilin *et al.*, Gate-tuneable and chirality-dependent charge-to-spin conversion in tellurium nanowires, Nat. Mater. **21**, 526 (2022).

[19] G. L. J. A. Rikken and N. Avarvari, Strong electrical magnetochiral anisotropy in tellurium, Phys. Rev. B **99**, 245153 (2019).

[20] X. Liu, I. Souza, and S. S. Tsirkin, Electrical magnetochiral anisotropy in trigonal tellurium from first principles, arXiv:2303.10164.

[21] P. He, S. S. L. Zhang, D. Zhu, Y. Liu, Y. Wang, J. Yu, G. Vignale, and H. Yang, Bilinear magnetoelectric resistance as a probe of three-dimensional spin texture in topological surface states, Nat. Phys. **14**, 495 (2018).

[22] D. C. Vaz, F. Trier, A. Dyrdał, A. Johansson, K. Garcia, A. Barthélémy, I. Mertig, J. Barnaś, A. Fert, and M. Bibes, Determining the Rashba parameter from the bilinear magnetoresistance response in a two-dimensional electron gas, Phys. Rev. Mater. **4**, 071001(R) (2020).

[23] P. He, S. S. L. Zhang, D. Zhu, S. Shi, O. G. Heinonen, G. Vignale, and H. Yang, Nonlinear planar Hall effect, Phys. Rev. Lett. **123**, 016801 (2019).

[24] C. Niu, G. Qiu, Y. Wang, P. Tan, M. Wang, J. Jian, H. Wang, W. Wu, and P. D. Ye, Tunable chirality-dependent nonlinear electrical responses in 2D tellurium, Nano Lett. **23**, 8445 (2023).

[25] S. H. Yang, R. Naaman, Y. Paltiel, and S. S. P. Parkin, Chiral spintronics, Nat. Rev. Phys. **3**, 328 (2021).

[26] R. Naaman, Y. Paltiel, and D. H. Waldeck, Chiral molecules and the electron spin, Nat. Rev. Chem. **3**, 250 (2019).

[27] T. A. Morgado, T. G. Rappoport, S. S. Tsirkin, S. Lannebère, I. Souza, and M. G. Silveirinha, Non-Hermitian linear electro-optic effect in three-dimensional materials, Phys. Rev. B **109**, 245126 (2024).

[28] M. Sakano, M. Hirayama, T. Takahashi, S. Akebi, M. Nakayama, K. Kuroda, K. Taguchi, T. Yoshikawa, K. Miayamoto, T. Okuda *et al.*, Radial spin texture in elemental tellurium with chiral crystal structure, Phys. Rev. Lett. **124**, 136404 (2020).

[29] Y. Wang, G. Qiu, R. Wang, S. Huang, Q. Wang, Y. Liu, Y. Du, W. A. Goddard III, M. J. Kim, X. Xu, P. D. Ye *et al.*, Field-effect transistors made from solution-grown two-dimensional tellurene, Nat. Electron. **1**, 228 (2018).

[30] See Supplemental Material at http://link.aps.org/supplemental/10.1103/PhysRevB.111.024405 for methods details, further experimental data, and detailed theoretical analysis, which includes Refs. [31–35].

[31] D. Hou, G. Su, Y. Tian, X. Jin, S. A. Yang, and Q. Niu, Multivariable scaling for the anomalous Hall effect, Phys. Rev. Lett. **114**, 217203 (2015).

[32] Y.-X. Huang, X. Feng, H. Wang, C. Xiao, and S. A. Yang, Intrinsic nonlinear planar Hall effect, Phys. Rev. Lett. **130**, 126303 (2023).

[33] Y.-X. Huang, Y. Wang, H. Wang, C. Xiao, X. Li, and S. A. Yang, Nonlinear current response of two-dimensional systems under in-plane magnetic field, Phys. Rev. B **108**, 075155 (2023).

[34] D. Kaplan, T. Holder, and B. Yan, Unification of nonlinear anomalous Hall effect and nonreciprocal magnetoresistance in metals by the quantum geometry, Phys. Rev. Lett. **132**, 026301 (2024).

[35] K. Das, S. Lahiri, R. B. Atencia, D. Culcer, and A. Agarwal, Intrinsic nonlinear conductivities induced by the quantum metric, Phys. Rev. B **108**, L201405 (2023).

[36] Y. Du, G. Qiu, Y. Wang, M. Si, X. Xu, W. Wu, and P. D. Ye, One-dimensional van der Waals material tellurium: Raman spectroscopy under strain and magneto-transport, Nano Lett. **17**, 3965 (2017).

[37] N. Zhang, G. Zhao, L. Li, P. Wang, L. Xie, B. Cheng, H. Li, Z. Lin, C. Xi, J. Ke *et al.*, Magnetotransport signatures of Weyl physics and discrete scale invariance in the elemental

semiconductor tellurium, Proc. Natl. Acad. Sci. USA **117**, 11337 (2020).

[38] M. Hirayama, R. Okugawa, S. Ishibashi, S. Murakami, and T. Miyake, Weyl node and spin texture in trigonal tellurium and selenium, Phys. Rev. Lett. **114**, 206401 (2015).

[39] J. Chen, T. Zhang, J. Wang, L. Xu, Z. Lin, J. Liu, C. Wang, N. Zhang, N. Zhang, S. P. Lau *et al.*, Topological phase change transistors based on tellurium Weyl semiconductor, Sci. Adv. **8**, eabn3837 (2022).

[40] S. V. Gallego, J. Etxebarria, L. Elcoro, E. S. Tasci, and J. M. Perez-Mato, Automatic calculation of symmetry-adapted tensors in magnetic and non-magnetic materials: A new tool of the Bilbao crystallographic server, Acta Crystallogr. **75**, 438 (2019).

[41] J. Xiong, S. K. Kushwaha, T. Liang, J. W. Krizan, M. Hirschberger, W. Wang, R. J. Cava, and N. P. Ong, Evidence for the chiral anomaly in the Dirac semimetal Na_3Bi, Science **350**, 413 (2015).

[42] A. V. Andreev and B. Z. Spivak, Longitudinal negative magnetoresistance and magnetotransport phenomena in conventional and topological conductors, Phys. Rev. Lett. **120**, 026601 (2018).

[43] Y. Gao, S. A. Yang, and Q. Niu, Intrinsic relative magneto-conductivity of nonmagnetic metals, Phys. Rev. B **95**, 165135 (2017).

[44] X. Dai, Z. Z. Du, and H. Z. Lu, Negative magnetoresistance without chiral anomaly in topological insulators, Phys. Rev. Lett. **119**, 166601 (2017).

[45] H. K. Pal, Quantum contribution to magnetotransport in weak magnetic fields and negative longitudinal magnetoresistance, Phys. Rev. B **105**, 075419 (2022).

[46] S. S. Tsirkin and I. Souza, On the separation of Hall and ohmic nonlinear responses, SciPost Phys. Core **5**, 039 (2022).

[47] A. Roy, F. T. Cerasoli, A. Jayaraj, K. Tenzin, M. Buongiorno Nardelli, and J. Slawińska, Long-range current- inducde spin accumulation in chiral crystals, npj Comput. Mater. **8**, 243 (2022).

[48] J. Kim and Y. Otani, Orbital angular momentum for spintronics, J. Magn. Magn. Mater. **563**, 169974 (2022).

[49] T. Yoda, T. Yokoyama, and Y. S. Murakami, Current-induced orbital and spin magnetizations in crystals with helical structure, Sci. Rep. **5**, 12024 (2015).

[50] Y.-X. Huang, C. Xiao, S. A. Yang, and X. Li, Scaling law for time-reversal-odd nonlinear transport, arXiv:2311.01219.